The Astronomical Journal, 152:193 (9pp), 2016 December doi:10.3847/0004-6256/152/6/193

K2-98b: A 32 $M_\oplus$ NEPTUNE-SIZE PLANET IN A 10 DAY ORBIT TRANSITING AN F8 STAR

Oscar Barragán[1], Sascha Grziwa[2], Davide Gandolfi[1,3], Malcolm Fridlund[4,5], Michael Endl[6], Hans J. Deeg[7,8], Manuel P. Cagigal[9], Antonino F. Lanza[10], Pier G. Prada Moroni[11,12], Alexis M. S. Smith[13], Judith Korth[2], Megan Bedell[14], Juan Cabrera[13], William D. Cochran[6], Felice Cusano[15], Szilard Csizmadia[13], Philipp Eigmüller[13], Anders Erikson[13], Eike W. Guenther[16], Artie P. Hatzes[16], David Nespral[7,8], Martin Pätzold[2], Jorge Prieto-Arranz[7,8], and Heike Rauer[13,17]

[1] Dipartimento di Fisica, Universitá di Torino, via P. Giuria 1, I-10125 Torino, Italy; oscar.barraganvil@edu.unito.it
[2] Rheinisches Institut für Umweltforschung an der Universität zu Köln, Aachener Strasse 209, D-50931 Köln, Germany
[3] Landessternwarte Königstuhl, Zentrum für Astronomie der Universität Heidelberg, Königstuhl 12, D-69117 Heidelberg, Germany
[4] Leiden Observatory, University of Leiden, PO Box 9513, 2300 RA, Leiden, The Netherlands
[5] Department of Earth and Space Sciences, Chalmers University of Technology, Onsala Space Observatory, SE-439 92 Onsala, Sweden
[6] Department of Astronomy and McDonald Observatory, University of Texas at Austin, 2515 Speedway, Stop C1400, Austin, TX 78712, USA
[7] Instituto de Astrofísica de Canarias, 38205 La Laguna, Tenerife, Spain
[8] Departamento de Astrofísica, Universidad de La Laguna, 38206 La Laguna, Spain
[9] Departamento de Física Aplicada, Universidad de Cantabria Avenida de los Castros s/n, E-39005 Santander, Spain
[10] INAF—Osservatorio Astrofisico di Catania, via S. Sofia 78, I-95123, Catania, Italy
[11] Physics Department "E. Fermi," University of Pisa, Largo B. Pontecorvo 3, I-56127, Pisa, Italy
[12] Istituto Nazionale di Fisica Nucleare, Largo B. Pontecorvo 3, I-56127, Pisa, Italy
[13] Institute of Planetary Research, German Aerospace Center, Rutherfordstrasse 2, D-12489 Berlin, Germany
[14] Department of Astronomy and Astrophysics, University of Chicago, 5640 S. Ellis Ave, Chicago, IL 60637, USA
[15] INAF—Osservatorio Astronomico di Bologna, Via Ranzani, 1, I-40127, Bologna, Italy
[16] Thüringer Landessternwarte Tautenburg, Sternwarte 5, D-07778 Tautenburg, Germany
[17] Center for Astronomy and Astrophysics, TU Berlin, Hardenbergstr. 36, D-10623 Berlin, Germany
Received 2016 August 2; revised 2016 September 20; accepted 2016 September 21; published 2016 November 29

ABSTRACT

We report the discovery of K2-98b (EPIC 211391664b), a transiting Neptune-size planet monitored by the *K2* mission during its Campaign 5. We combine the *K2* time-series data with ground-based photometric and spectroscopic follow-up observations to confirm the planetary nature of the object and derive its mass, radius, and orbital parameters. K2-98b is a warm Neptune-like planet in a 10 day orbit around a $V = 12.2$ mag F-type star with $M_\star = 1.074 \pm 0.042\ M_\odot$, $R_\star = 1.311^{+0.083}_{-0.048}\ R_\odot$, and age of $5.2^{+1.2}_{-1.0}$ Gyr. We derive a planetary mass and radius of $M_\mathrm{p} = 32.2 \pm 8.1\ M_\oplus$ and $R_\mathrm{p} = 4.3^{+0.3}_{-0.2}\ R_\oplus$. K2-98b joins the relatively small group of Neptune-size planets whose mass and radius have been derived with a precision better than 25%. We estimate that the planet will be engulfed by its host star in ~3 Gyr, due to the evolution of the latter toward the red giant branch.

Key words: planets and satellites: detection – planets and satellites: individual K2-98b (EPIC 211391664b) – stars: fundamental parameters

1. INTRODUCTION

The transit of an exoplanet in front of its host star provides us with valuable information about its size. When combined with radial velocity (RV) measurements (e.g., Mayor & Queloz 1995) or transit timing variations (e.g., Ford et al. 2011), transit photometry gives us access to the geometry of the orbit, enabling the measurement of the true mass of the planet, its radius, and consequently its mean density. Masses, radii, densities, and orbital parameters are fundamental "ingredients" to study the internal structure, composition, dynamical evolution, tidal interaction, architecture, and atmosphere of exoplanets (e.g., Winn & Fabrycky 2015; Hatzes 2016).

The space-based photometry revolution of *CoRoT* (Baglin et al. 2006) and *Kepler* (Borucki et al. 2010) has given us access to the small-radius planet domain ($R_\mathrm{p} \lesssim 6\,R_\oplus$, i.e., Neptune- and Earth-size planets), a regime that is not easily accessible from the ground. Neptune-like planets ($2.0 \lesssim R_\mathrm{p} \lesssim 6.0\,R_\oplus$, $10 \lesssim M_\mathrm{p} \lesssim 40\,M_\oplus$ Borucki et al. 2011) are of special interest as they mark the transition from Super-Earths to larger planets with higher volatile content, more akin to the icy giants in our solar system. However, our knowledge of these planets is still quite limited. Although *Kepler* has found that ~26% of Sun-like stars in our Galaxy host small planets with orbital period shorter than 100 days (Marcy et al. 2014), determinations of masses with a precision of ~25%—or better—have been possible only for a few dozen Neptune-like planets.[18] This is because of the small RV variations induced by such planets and the faintness of most of the *Kepler* host stars ($V > 13$ mag), which does not make them suitable for precise RV follow-up observations.

In its extended *K2* mission, *Kepler* is surveying different stellar fields located along the ecliptic, performing 80 day long continuous observations of 10,000–20,000 stars per campaign. *K2* data products have no proprietary period and are released to the community typically three months after the end of each campaign, enabling immediate follow-up observations. The *K2* mission is an unique opportunity to gain knowledge of transiting Neptune-sized planets (e.g., David et al. 2016; Espinoza et al. 2016). *K2* is targeting a number of bright dwarfs ($V \leqslant 12$ mag) higher than the original *Kepler* mission (Howell et al. 2014). This is a definitive advantage for any RV follow-up observations.

As part of the KEST, ESPRINT, and PICK2 collaborations (Cochran et al. 2015; Grziwa et al. 2015; Sanchis-Ojeda

[18] As of 2016 June; source: exoplanet.org.

et al. 2015; Johnson et al. 2016; Nespral et al. 2016), we have recently started an RV follow-up program that aims at confirming Neptune-size candidates detected by the *K2* mission and at measuring their masses via high-precision RV follow-up observations. We herein report the discovery of K2-98b (EPIC 211391664b) a transiting Neptune-size planet in a 10 day orbit around a relatively bright ($V = 12.2$ mag) solar-like star photometrically monitored by the *K2* mission during its Campaign 5. We combine the *K2* photometry with ground-based follow-up observations to assess the planetary nature of the transiting object and derive its mass. We note that K2-98b has been recently identified as a planet candidate by Pope et al. (2016) and Barros et al. (2016), but has not previously been confirmed. We are the first team to confirm and characterize this planetary system in detail.

The paper is organized as follows: in Section 2 we present the *K2* photometry, and in Sections 3 and 4 our ground-based photometric and spectroscopic follow-up, respectively. Section 5 reports on the characterization of the host star. Section 6 describes the joint RV and photometric analysis. The results, discussion, and conclusion are given in Sections 7 and 8.

2. *K2* LIGHT CURVE

K2 Campaign 5 observations began on 2015 April 27 UT and lasted until 2015 July 10 UT.[19] During the observations, the boresight of the *Kepler* spacecraft was pointed at coordinates $\alpha = 08^{h}\,40^{m}\,38^{s}$, $\delta = +16^{\circ}\,49'47''$. A total of 26,054 light curves were simultaneously acquired by *K2*: 25,850 in long cadence mode (~30 minute integration time) and 204 in short cadence mode (~1 minute integration time).

In this work, we use the light curves extracted by Vanderburg & Johnson (2014).[20] These were the only publicly available light curves at the time we started the detection of transiting planet candidates in *K2* Field 5. We search the light curves for transit signals using the DST algorithm (Cabrera et al. 2012) and the EXOTRANS pipeline (Grziwa et al. 2012). DST and EXOTRANS have been applied extensively to both *CoRoT* (Cabrera et al. 2009; Carone et al. 2012; Carpano et al. 2009; Cavarroc et al. 2012; Erikson et al. 2012) and *Kepler* (Cabrera et al. 2014; Grziwa & Pätzold 2016) data. All transit detection algorithms search for a pattern in the data and use statistics to assess whether a signal is present in the data or not. When compared to widely used algorithms such as, e.g., Box Least Squares (BLS; Kovács et al. 2002), DST uses an optimized transit shape, with the same number of free parameters as BLS, and an optimized statistic for signal detection. EXOTRANS uses a combination of the wavelet based filter technique VARLET (Grziwa & Pätzold 2016) and the BLS detection algorithm. VARLET was developed to reduce both stellar variability and data discontinuities. EXOTRANS calculates the Signal Detection Efficiency (SDE) for every light curve when the BLS algorithm is used. The Generalized Extreme Value distribution is used to calculate the SDE threshold (Grziwa et al. 2012). We consider all light curves with an SDE value higher than the SDE threshold for further inspection (about 4% of the sample).

Both DST and EXOTRANS identify a periodic transit-like signal associated with the target EPIC 211391664. The star was proposed for *K2* observations by programs GO5007 (P.I.: J. Winn) and GO5029 (P.I.: D. Charbonneau). For brevity we will hereafter refer to the star and its transiting planet as K2-98 and K2-98b, respectively.

The target passes all of the tests that we carry out to identify likely false positives with the DST and EXOTRANS pipelines. These tests were regularly used during the *CoRoT* mission. Briefly, we stack and fit even and odd transits separately using the Transit Analysis package TAP (Gazak et al. 2012). We find neither significant odd–even transit depth variations nor ellipsoidal variability/tidal deformation signatures in the light curve, both typically observed in eclipsing binaries. We also find no shallow secondary eclipses that might suggest an eclipsing binary scenario. Possible secondary eclipses are simulated using the detached eclipsing binary light curve fitter (DEBIL; Devor 2005) we first described in Pätzold et al. (2012). Similar tests are performed using the DST pipeline and are described in Cabrera et al. (2009, 2012). Large photometric variation in phase with the candidate orbital period is a hint for a possible binary. Such variations are also not found, and so we proceed to a more detailed fitting of the light curve, as well as high-resolution imaging, reconnaissance spectroscopy, and RV observations (Sections 3 and 4).

We also search the *K2* light curve of K2-98 for additional transit signals, but none are found. The main identifiers, optical and infrared magnitudes, and proper motions of this star are listed in Table 1.

Table 1
Main Identifiers, Magnitudes, and Proper Motion of K2-98

Parameter	Value	Source
Main Identifiers		
EPIC	211391664	EPIC
UCAC	508-047859	EPIC
2MASS	08255719+1130402	EPIC
α(J2000.0)	$08^{h}05^{m}57\overset{s}{.}189$	EPIC
δ(J2000.0)	$+11^{\circ}30'\,40\overset{''}{.}12$	EPIC
Magnitudes		
B	12.646 ± 0.030	EPIC
V	12.166 ± 0.030	EPIC
g	12.313 ± 0.030	EPIC
r	12.031 ± 0.030	EPIC
J	11.124 ± 0.022	2MASS
H	10.905 ± 0.025	2MASS
K	10.869 ± 0.028	2MASS
*W*1	10.823 ± 0.023	*WISE*
*W*2	10.856 ± 0.020	*WISE*
*W*3	10.678 ± 0.108	*WISE*
*W*4	8.258	*WISE*
Proper motions		
$\mu_\alpha \cos\delta$ (mas yr^{-1})	−15.4 ± 2.3	UCAC2
μ_δ(mas yr^{-1})	−8.8 ± 1.5	UCAC2

Notes. Values of fields marked with EPIC are taken from the Ecliptic Plane Input Catalog, available at http://archive.stsci.edu/k2/epic/search.php. Values marked with UCAC2, 2MASS, and *WISE* are from Zacharias et al. (2004) and Cutri et al. (2003, 2013), respectively. The *WISE W*4 magnitude is an upper limit.

3. FASTACAM HIGH-RESOLUTION IMAGING

We observed K2-98 on 2016 May 17 with the FASTCAM lucky imaging camera (Oscoz et al. 2008) mounted on the

[19] See http://keplerscience.arc.nasa.gov/k2-fields.html.
[20] Publicly available at https://www.cfa.harvard.edu/~avanderb/allk2c5obs.html.

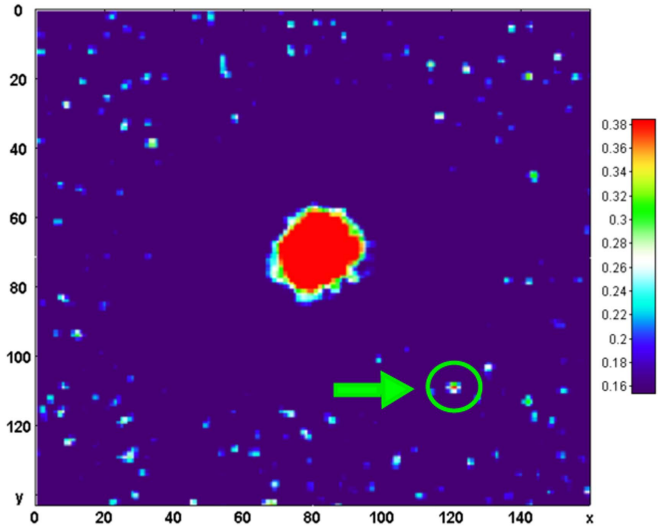

Figure 1. FASTCAM image of K2-98 processed with COELI. The pixel scale is 0.″042; north is left, east is down. K2-98 is at the center of the ring-shaped feature, which is an artifact of the image processing. The faint nearby star 1.″9 southeast of K2-98 is indicated with a green arrow. Colors from blue to red represent the increasing level of temporal covariance with the central target, following the data processing with COELI.

1.5 m Carlos Sánchez Telescope of Teide Observatory in Tenerife (Spain). To account for the low altitude of the object at the time of our observation, we used a relatively long exposure time of 300 mas and acquired a total of 5000 images. The integration time of 300 mas does not completely freeze the atmosphere, but this duration was necessary to collect enough light to detect faint objects. We selected the 300 best images, i.e., those with the highest Strehl ratio, and processed the data using the COELI[21] algorithm (Cagigal et al. 2016). COELI provides a map of the temporal covariance between the intensity of K2-98 and the intensity of the remaining pixels (Figure 1). This removes the speckled halo surrounding the host star and creates a dark ring-shaped region around it, which is the zone where the algorithm is more sensitive to the presence of faint objects (Cagigal et al. 2016). COELI also reinforces in this zone those pixels whose intensity follows the same temporal fluctuations as K2-98, which can only happen when the pixels contain an object. We estimate that in the ring-shaped region, at distances of 0.″–1.″7, there are no background objects brighter than $V \approx 19$ mag (i.e., $\Delta V \approx 7$ mag).

The final image shows the target to be isolated except for the detection of an object located 1.″9 southwest of K2-98. The detected object is located just outside the dark ring-shaped region, in a zone where COELI provides relatively poor contrast and small spots show arbitrarily amplified noise. Nevertheless, due to being rather bright, we consider the source as a secure detection, and estimate it to be 50 ± 10 times fainter (4.2 ± 0.2 mag) than the main target. The distance of 1.″9 between the target and the faint object is less than the sky-projected size of the *Kepler*/*K2* CCD pixel (∼4″). We therefore assume that the light from the faint object contributes with a fraction of $1/(50 \pm 10)$ to the measured flux of K2-98 and correct the *K2* light curve accordingly prior to performing the joint analysis presented in Section 6.

No additional contaminants are identified. The DSS images reveal that the next closest star with a brightness comparable to the target is a ∼3.5 mag fainter object that is located ∼42″ east of K2-98, which is too large to produce any relevant influence on the *K2* light curve of K2-98.

[21] ImageJ Plugin available at https://imagej.nih.gov/ij/plugins/index.html.

4. SPECTROSCOPIC FOLLOW-UP OBSERVATIONS

We took two reconnaissance spectra of K2-98 with the Harlan J. Smith 2.7 m Telescope and the Tull Coudé Spectrograph (Tull et al. 1995) at the McDonald Observatory. The Tull spectrograph covers the entire optical spectrum (3450–9800 Å) at a resolving power of $R \approx 60{,}000$. We used exposure times of 1800 s, which resulted in a signal-to-noise ratio (S/N) of ∼30 per pixel at 5500 Å. We derived a first estimate of the spectroscopic parameters by using our code Kea that compares observed high-resolution spectra to a large library of synthetic models (Endl & Cochran 2016). For the first spectrum, we obtain the following parameters: $T_{\rm eff} = 5880 \pm 107$ K, $\log g_\star = 3.81 \pm 0.31$ (cgs), [Fe/H] $= -0.06 \pm 0.07$ dex, and a $v \sin i_\star = 8.8 \pm 0.3$ km s^{-1}. For the second observation, $T_{\rm eff} = 5820 \pm 116$ K, [Fe/H] $= -0.03 \pm 0.08$ dex, $\log g_\star = 4.00 \pm 0.35$ (cgs), and a $v \sin i_\star = 8.7 \pm 0.4$ km s^{-1}. We also measure an absolute RV of 76.7 ± 0.2 km s^{-1} by cross-correlating the data with spectra of the RV standard star HD 50692 (Udry et al. 1999).

We also acquired four high-resolution spectra ($R \approx 67{,}000$) in 2015 November and 2016 January using the FIbre-fed Échelle Spectrograph (FIES; Frandsen & Lindberg 1999; Telting et al. 2014) mounted at the 2.56 m Nordic Optical Telescope (NOT) at Roque de los Muchachos Observatory (La Palma, Spain). We adopted the observing strategy described in Buchhave et al. (2010) and Gandolfi et al. (2013, 2015), i.e., we took three consecutive exposures of 1200 s per observation epoch—to remove cosmic-ray hits—and acquired long-exposed ($T_{\rm exp} \approx 35$ s) ThAr spectra immediately before and after the three sub-exposures—to trace the RV drift of the instrument. We reduced the data using standard IRAF and IDL routines. The S/N of the extracted spectra is ∼30 per pixel at 5500 Å. RV measurements were derived via multi-order cross-correlation with the RV standard star HD 50692—observed with the same instrument set-up as K2-98. They are listed in Table 2 along with the FWHM and bisector span (BIS) of the cross-correlation function (CCF).

We also acquired eight high-resolution spectra using the HARPS ($R \approx 115{,}000$; Mayor et al. 2003) and HARPS-N spectrographs ($R \approx 115{,}000$; Cosentino et al. 2012) mounted at the ESO-3.6 m telescope at La Silla observatory (Chile) and the 3.58 m Telescopio Nazionale Galileo (TNG) at the Roque de los Muchachos Observatory (La Palma, Spain), respectively. The observations were performed between 2015 December and 2016 May, setting the exposure times to 1800–3600 s depending on the sky condition. We monitored the moon background light using the second fiber and reduced the data with the dedicated HARPS and HARPS-N data reduction software pipeline. The S/N of the extracted spectra is S/N = 35–45 per pixel at 5500 Å. Radial velocities (Table 2) were extracted by cross-correlation with a G2 numerical mask (Baranne et al. 1996; Pepe et al. 2002).

We search for possible correlations between the RVs and the CCF FWHM, as well as between the RVs and CCF BIS. By combining all the three data sets, we derive for the RV and BIS data a Pearson correlation coefficient of −0.36 with a *p*-value of 0.25, while for the RV and FWHM measurements we obtain a Pearson correlation coefficient of −0.32 with a *p*-value of

Table 2
Radial Velocity Measurements of K2-98

BJD_{TDB} −2450000	RV (km s^{-1})	σ_{RV} (km s^{-1})	CCF FWHM (km s^{-1})	CCF BIS (km s^{-1})
FIES				
7342.706590	76.6027	0.0082	15.1659	0.0390
7344.744082	76.6243	0.0081	15.1694	0.0401
7347.706247	76.6143	0.0082	15.1770	0.0430
7394.699773	76.6130	0.0082	15.1790	0.0366
HARPS				
7509.495449	76.7558	0.0084	10.3567	0.0430
7511.495428	76.7516	0.0053	10.3617	0.0442
7512.472984	76.7376	0.0055	10.3632	0.0450
7516.525371	76.7425	0.0068	10.3729	0.0600
HARPS-N				
7371.582060	76.7393	0.0077	10.3474	0.0407
7371.601679	76.7324	0.0098	10.3309	0.0499
7448.440479	76.7499	0.0074	10.3352	0.0456
7512.429111	76.7313	0.0048	10.3558	0.0580

0.31. The lack of significant correlations at a 0.05 confidence level provides further evidence that the observed RV variations are caused by the orbital motion of the planet rather than stellar activity. It also excludes the presence of an unseen stellar contaminant whose CCF is blended with the CCF of K2-98. We also perform a visual inspection of the Tull, FIES, HARPS, and HARPS-N spectra and search the CCFs for the presence of a secondary peak. We find no significant evidence of a second set of spectral lines in the data.

5. PROPERTIES OF THE HOST STAR

We co-add the spectra from the NOT, ESO-3.6 m, and TNG separately to get a combined FIES spectrum, a separate combined HARPS spectrum, and a third separate HARPS-N spectrum. The co-added data have a S/N of ∼100 per pixel at 5500 Å. We use the three combined spectra to refine the estimates of the spectroscopic parameters of the host star. Following the spectral analysis of *CoRoT* and *Kepler* host stars (e.g., Fridlund et al. 2010; Gandolfi et al. 2010, 2015), we select spectral features that are sensitive to different photospheric parameters. Our method is based on Spectroscopy Made Easy (SME), a software package that calculates synthetic spectra and fits them to high-resolution observed spectra (Valenti & Piskunov 1996). SME is especially designed to determine basic stellar and atomic parameters from a match of the observed and normalized spectrum to the synthetic spectra generated from the parameterized atmospheres. It uses a nonlinear least squares algorithm to solve for any subset of allowed parameters, which include atomic data ($\log gf$ and van der Waals damping constants), the model atmosphere parameters ($T_{\rm eff}$, $\log g_\star$), metal abundances, and projected rotational velocity $v \sin i_\star$. The SME 4.43 distribution includes a grid with a very large set of 1D-LTE plane-parallel stellar atmospheric models (ATLAS9, ATLAS12, NextGen, and MARCS models; Kurucz 1993, p. 13; 2013; Hauschildt et al. 1999; Gustafsson et al. 2008). ATLAS12 is an opacity sampling model atmosphere program that computes the same models as ATLAS9 but instead of using pretabulated opacities and models with arbitrary abundances, ATLAS12 uses individual abundances and line data.

Our spectral analysis begins by primarily using the wings of the H_α and H_β Balmer lines to determine $T_{\rm eff}$, adopting the calibration equations of Bruntt et al. (2010) and Doyle et al. (2014) to estimate the microturbulent ($V_{\rm mic}$) and macroturbulent ($V_{\rm mac}$) velocities. The projected rotational velocity $v \sin i_\star$ is determined from a set of iron lines after which Mg I lines at $\lambda = 5167$, 5173, and 5184 Å and Ca I lines at $\lambda = 6102$, 6122, 6162, and 6439 Å are used to estimate the surface gravity $\log g_\star$. In order to verify the accuracy of this method, we analyze a solar spectrum from Wallace et al. (2011). Comparing with the discussion given in Valenti & Fischer (2005), we find the errors quoted there to be representative of what can currently be achieved when calculating synthetic spectra in order to fit high-resolution, high S/N spectra.

We obtain stellar parameters from the FIES, HARPS, and HARPS-N consistent to within 1σ uncertainties. Our final adopted values for $T_{\rm eff}$, $\log g_\star$, [M/H], and $v \sin i_\star$ are the weighted means of the values produced by the three co-added spectra and the quoted errors are the 1σ standard deviation. They are also consistent to within 2σ with the preliminary values derived from the two reconnaissance spectra taken at the McDonald observatory (Section 4). We note that the $v \sin i_\star$ estimates obtained from the Tull spectroscopic data using KEA should be regarded as upper limits as they do not account for the line broadening induced by the macroturbulent velocity (Endl & Cochran 2016).

We determine the stellar mass, radius, and age by combining the effective temperature $T_{\rm eff}$ and metallicity [M/H] with the mean density $\rho_\star$ obtained from the transit light curve modeling (Section 6). We compare the position of the host star on a $\rho_\star$ versus $T_{\rm eff}$ with a fine grid of evolutionary tracks. The latter are computed ad hoc for this work using the FRANEC code (Tognelli et al. 2011), setting the same configuration as for the Pisa stellar evolution database for low-mass stars[22] (Dell'Omodarme et al. 2012). We adopt the mixing-length parameter $\alpha_{ml} = 1.74$, which is our solar calibrated value for the heavy element mixture of the Sun by Asplund et al. (2009). We account for microscopic diffusion by means of the routine developed by Thoul et al. (1994). The final grid contains tracks in the mass range 0.90–1.30 $M_\odot$, with a step of 0.01 $M_\odot$, computed for five different couples of initial metallicity Z and helium abundance Y, namely, (0.006, 0.260), (0.008, 0.265), (0.010, 0.268), (0.011, 0.271), (0.012, 0.273), and (0.013, 0.274). We find that evolutionary models with initial metal content between $Z = 0.011$ and $Z = 0.013$ reproduce the current photospheric metallicity. With a mass of $M_\star = 1.074 \pm 0.042\ M_\odot$, radius of $R_\star = 1.311^{+0.083}_{-0.048}\ R_\odot$, and an age of $5.2^{+1.2}_{-1.0}$ Gyr (Table 3), K2-98 is a slightly evolved star leaving the main sequence. Based on the calibration of Straizys & Kuriliene (1981) for dwarf stars, the effective temperature of the star translates into an F8 V spectral type. The stellar mass and radius imply a surface gravity of $\log g_\star = 4.23^{+0.03}_{-0.05}$ (cgs), which agrees within 1σ with the value of $\log g_\star = 4.35 \pm 0.10$ (cgs) derived from the co-added spectra.

We check the *K2* data for evidence of rotational modulation. The lack of significant periodic and quasi-periodic photometric variation prevents us from estimating the stellar rotation period. Assuming that the star is seen equator-on, the projected rotational velocity $v \sin i_\star = 6.1 \pm 0.5$ km s^{-1} and stellar radius $R_\star = 1.311^{+0.083}_{-0.048}\ R_\odot$ imply a rotational period of $P_{\rm rot} = 10.9^{+1.0}_{-0.8}$ days.

[22] Available at http://astro.df.unipi.it/stellar-models/.

Table 3
Stellar and Planetary Parameters

Parameter	Value
Model Parameters	
Orbital period $P_{\rm orb}$ (days)	10.13675 ± 0.00033
Transit epoch T_0 ($\rm BJD_{TDB}-2450000$)	7145.9807 ± 0.0012
Scaled semimajor axis $a/R_\star$	$15.388^{+0.543}_{-1.192}$
Scaled planet radius $R_{\rm p}/R_\star$	$0.0301^{+0.0004}_{-0.0003}$
Impact parameter, b	$0.27^{+0.17}_{-0.14}$
Parameterized limb-darkening coefficient q_1[a]	0.40 ± 0.05
Parameterized limb-darkening coefficient q_2[a]	0.26 ± 0.05
Eccentricity e	0 (fixed)
Radial velocity semi-amplitude variation K ($\rm m\ s^{-1}$)	9.1 ± 2.3
Systemic velocity $\gamma_{\rm FIES}$ ($\rm km\ s^{-1}$)	76.6116 ± 0.0029
Systemic velocity $\gamma_{\rm HARPS}$ ($\rm km\ s^{-1}$)	76.7479 ± 0.0022
Systemic velocity $\gamma_{\rm HARPS-N}$ ($\rm km\ s^{-1}$)	76.7417 ± 0.0026
Derived parameters	
Semimajor axis of the planetary orbit a (au)	$0.0943^{+0.0061}_{-0.0052}$
Transit duration τ_{14} (hr)	$5.03^{+0.05}_{-0.04}$
Transit ingress/egress duration $\tau_{12} = \tau_{34}$ (hr)	$0.16^{+0.03}_{-0.01}$
Orbit inclination along the line of sight $i_{\rm p}$ (°)	$89.0^{+0.5}_{-0.7}$
Stellar parameters	
Star mass $M_\star$ ($M_\odot$)	1.074 ± 0.042
Star radius $R_\star$ ($R_\odot$)	$1.311^{+0.083}_{-0.048}$
Surface gravity $\log g_\star$ (cgs)[b]	$4.23^{+0.03}_{-0.05}$
Mean density $\rho_\star$ ($\rm g\ cm^{-3}$)	$0.66^{+0.07}_{-0.12}$
Star age (Gyr)	$5.2^{+1.2}_{-1.0}$
Spectral type[c]	F8 V
Effective temperature $T_{\rm eff}$ (K)	6120 ± 80
Iron abundance [Fe/H] (dex)	-0.2 ± 0.1
Nickel abundance [Ni/H] (dex)	-0.1 ± 0.1
Silicon abundance [Si/H] (dex)	-0.1 ± 0.1
Calcium abundance [Ca/H] (dex)	-0.1 ± 0.1
Sodium abundance [Na/H] (dex)	-0.0 ± 0.1
Magnesium abundance [Mg/H] (dex)	-0.0 ± 0.1
Microturbulent velocity $v_{\rm mic}$[c]	1.3 ± 0.1
Macroturbulent velocity $v_{\rm mac}$[d]	3.7 ± 0.6
Projected rotational velocity $v \sin i_\star$	6.1 ± 0.5
Distance d (pc)	435^{+30}_{-15}
Visual interstellar extinction $A_{\rm v}$ (mag)	0.05 ± 0.05
Planetary parameters	
Planet mass $M_{\rm p}$ ($M_\oplus$)	32.2 ± 8.1
Planet radius $R_{\rm p}$($R_\oplus$)	$4.3^{+0.3}_{-0.2}$
Planet density $\rho_{\rm p}$ ($\rm g\ cm^{-3}$)	$2.15^{+0.67}_{-0.60}$
Equilibrium temperature $T_{\rm eq}$ (K)	1102^{+26}_{-20}

Notes. The adopted Sun and Earth units follow the recommendations from the International Astronomical Union (Prsa et al. 2016).
[a] The limb-darkening coefficient parameterization follows Kipping (2013). The estimates have been obtained assuming $u_1 = 0.33 \pm 0.06$ and $u_2 = 0.30 \pm 0.06$ for the linear and quadratic limb-darkening coefficients (Claret & Bloemen 2011), adopting 20% conservative error bars.
[b] Stellar surface gravity $\log g_\star$ as measured from the global fit and evolutionary tracks. The spectroscopic analysis gives $\log g_\star = 4.35 \pm 0.10$ (cgs).
[c] Based on the spectral type versus effective temperature calibration of Straizys & Kuriliene (1981) for dwarf stars.
[d] Micro- and macroturbulent velocities from the calibration equations of Bruntt et al. (2010) and Doyle et al. (2014), respectively.

Following the technique described in Gandolfi et al. (2008), we use the magnitudes listed in Table 1 and our spectroscopic parameters to estimate the interstellar extinction and distance to the star. We find that the light of K2-98 suffers a negligible reddening ($A_{\rm v} = 0.05 \pm 0.05$ mag) and the star is located at a distance $d = 435^{+30}_{-15}$ pc from the Sun.

6. JOINT RV-TRANSIT MODELING

We perform the joint modeling of the photometric and spectroscopic data using the code `pyaneti`, a Python/Fortran software suite that finds the best-fitting solution using Markov Chain Monte Carlo (MCMC) methods based on Bayesian inference (O. Barragán et al. 2016, in preparation). The code implements ensemble sampling with affine invariance for a larger coverage of parameter space (Goodman & Weare 2010).

The photometric data included in the joint analysis are subsets of the whole *K2* light curve. We select ∼13 hr of data points centered on each of the seven transits[23] observed by *K2*. We detrend the individual transits using a second-order polynomial locally fitted to the ∼16 out-of-transit points per transit (8 points per side). The final data set contains 180 photometric points. The modeled RV data set contains the 12 measurements listed in Table 2.

The RV model is given by a Keplerian orbit and an offset term for each systemic velocity (see, e.g., Perryman 2014). We fit for the systemic velocity γ_j (as measured by the jth instrument), the RV semi-amplitude variation K, the transit epoch T_0, the period $P_{\rm orb}$, the eccentricity e, and the argument of periastron of the star's orbit ω measured from the ascending node to its periastron.

The transit model follows the quadratic limb-darkened law of Mandel & Agol (2002). We account for the *K2* long integration ($T_{\rm exp} = 29.425$ minutes) by supersampling the transit model with 10 sub-samples per long cadence data (Kipping 2010). For the linear u_1 and quadratic u_2 limb-darkening coefficients, we use the $q_1 = (u_1 + u_2)^2$ and $q_2 = u_1\,[\,2(u_1 + u_2)]^{-1}$ parameterization described in Kipping (2013). The fitted transit parameters are T_0, $P_{\rm orb}$, e, ω, q_1, q_2, scaled semimajor axis $a/R_\star$, planet-to-star radius ratio $R_p/R_\star$, and impact parameter b.

We use the Gaussian likelihood

$$\mathcal{L} = (2\pi)^{-n/2}\left[\prod_{i=1}^{n}\sigma_i\right]\exp\left[-\sum_{i=1}^{n}\frac{(D_i - M_i)^2}{2\sigma_i^2}\right], \qquad (1)$$

where $n = n_{\rm tr} + n_{\rm RV}$ is the number of transit and RV points, and σ_i is the error associated to each data point D_i, and M_i is the model associated to a given D_i.

We fit for both a circular and an eccentric model. The joint modeling is carried out by running 500 independent chains with uninformative uniform priors in the wide ranges $P_{\rm orb} = [10.1,\ 10.2]$ days, $T_0 = [2457145.7,\ 2457146.3]$, $b = [0,\ 1]$, $a/R_\star = [5,\ 100]$, $R_{\rm p}/R_\star = [0.005,\ 0.2]$, $K = [0.001,\ 1.0]\,\rm km\,s^{-1}$, and $\gamma_j = [1,\ 100]\,\rm km\,s^{-1}$. For the circular model we set $e = 0$ and $\omega = 90$ deg, while for the eccentric fit we set uninformative uniform priors between the limits $e = [0, 1]$ and $\omega = [0, 360]$ deg. For q_1 and q_2 we set uninformative uniform priors in the range [0, 1] to sample a physical solution for the limb-darkening coefficients (Kipping 2013).

We check the chain convergence by comparing the "between-chain" and "within-chain" variance using the Gelman-Rubin statistics. The burning-in phase used 25,000 additional iterations with a thin factor of 50, leading to a final

[23] The transit duration is ∼5 hr.

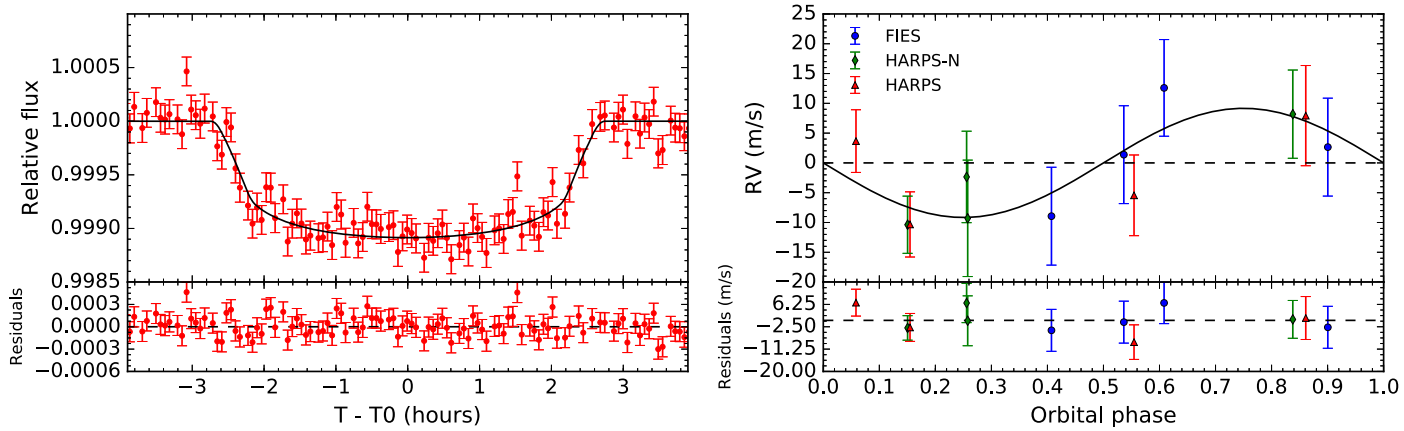

Figure 2. Left panel: transit light curve folded to the orbital period of K2-98b and residuals. The red points are the *K2* data and their error bars. The solid line marks the re-binned best-fitting transit model. Right panel: phase-folded FIES (blue circles), HARPS-N (green diamonds), and HARPS (red triangles) RV measurements of K2-98b and best-fitting circular orbit (solid line), following the subtraction of the systemic velocities as measured from each instrument.

number of 500 independent points for each chain, i.e., 250,000 independent points for each fitted parameter.

An initial global fit to the data yields the parameterized limb-darkening coefficients $q_1 = 0.27^{+0.29}_{-0.12}$ and $q_2 = 0.47^{+0.26}_{-0.24}$, which corresponds to $u_1 = 0.47^{+0.14}_{-0.17}$ and $u_2 = 0.03^{+0.36}_{-0.21}$. As described in Csizmadia et al. (2013), the large uncertainties arise from the shallow transit depth (∼0.1%), the small number of data points (∼180) and transits (7), and the *K2* long integration time (∼30 minutes). We thus choose to constrain the limb-darkening coefficient by interpolating the table of Claret & Bloemen (2011) and assuming conservative 20% error bars. We stress that the system parameters derived with uninformative priors on the limb-darkening coefficients are consistent to within 1σ uncertainties with those obtained by constraining u_1 and u_2.

7. RESULTS AND DISCUSSION

Figure 2 shows the folded transit light curves and phase-folded RV curve, along with their best-fitting models. The parameter estimates and error bars are listed in Table 3. They are taken as the median and the 68% central interval of the final posterior distributions (Gregory 2010). Our results are consistent with the transit parameters derived by Pope et al. (2016) and Barros et al. (2016).

Our RV measurements do not allow us to constrain the eccentricity of the system. A fit for an eccentric orbit yields $0.19^{+0.17}_{-0.13}$ with a significance of only about 1σ. In order to further check whether the non-zero eccentricity solution is significant or not, we run an F-test and calculate the *p*-value, i.e., the probability that the apparent eccentricity could have arisen if the underlying orbit were circular (Lucy & Sweeney 1971). In doing so we take into account the number of fitted parameters—both for the circular and eccentric model, the number of measurements and their uncertainties, and the residuals from the best-fitting circular and eccentric solution. We find a *p*-value of 0.87, which is much higher than the 0.05 significance threshold suggested by Lucy & Sweeney (1971), to prefer $e \neq 0$ over $e = 0$. We therefore conclude that the non-zero best-fitting eccentricity obtained with models where e is allowed to vary is not significant. Moreover, we find that the circular (dof = 153) and eccentric (dof = 151) models provide very similar minimum χ^2 values of ∼152. The difference of the Bayesian information criterion is $\Delta\mathrm{BIC} = 10$ between the two models, implying that the circular model is favored. We therefore adopt the circular model as the one that better describes our data. We note that the derived system parameters for a non-zero eccentricity are consistent to within 1σ uncertainties with those derived assuming a circular orbit.

K2-98b has a mass of $M_\mathrm{p} = 32.2 \pm 8.1\ M_\oplus$ and a radius of $R_\mathrm{p} = 4.3^{+0.3}_{-0.2}\ R_\oplus$, consistent with a density of $2.15^{+0.67}_{-0.60}$ g cm^{-3}. These parameters are calculated by adopting the stellar mass and radius derived in Section 5 and listed in Table 3. Figure 3 shows the position of K2-98b in the mass–radius diagram for Neptune-size planets. The plot includes only those objects whose mass and radius have both been estimated with a precision of at least ∼25%. K2-98b joins the family of intermediate mass ($20 < M_\mathrm{p} < 50\ M_\oplus$) Neptune-size planets. Whereas its radius is slightly larger than that of Neptune ($3.9\ R_\oplus$), the mass of K2-98b is almost twice as large as the mass of Neptune. This implies that a solid massive core surrounded by a large atmosphere is expected (see, e.g., Weiss & Marcy 2014).

Assuming a minimum mass solar nebula (MMSN), the isolation mass (Schlichting 2014) of a planet at 0.093 au is $\sim 0.004\ M_\oplus$, which is significantly lower than the mass of K2-98b. In order to form K2-98b in situ, a disk surface density ∼5500 times larger than the MMSN is required. This value would generate gravitational instabilities in the disk because its Toomre parameter would be $Q \approx 0.03 \ll 1$ (Schlichting 2014). This scenario does not support the in situ formation of K2-98b.

Valsecchi et al. (2014) proposed that Neptune-mass planets may form via migration of hot Jupiters that come so close to their host stars as to fill their Roche lobe and start conservative mass transfer to the star. This may reverse the direction of migration and increase the orbital period. However, it seems very difficult to reach a final orbital period of about 10 days, as in the case of K2-98b. Moreover, this formation scenario cannot easily account for the measured relatively low density of the planet ($2.15^{+0.67}_{-0.60}$ g cm^{-3}). Therefore, we argue that K2-98b likely formed in the outer region of the protoplanetary disk and then migrated inwards to its current position (see, e.g., Kley & Nelson 2012).

We integrate the equations of tidal and rotational evolution as in Lanza & Mathis (2016) assuming a constant modified tidal quality factor $Q'_\star$ for the star. Given that the stellar rotation period is close to the orbital period (Section 5), tidal dissipation by inertial waves inside the star is considered to lead to a remarkably stronger tidal interaction than in the case of the

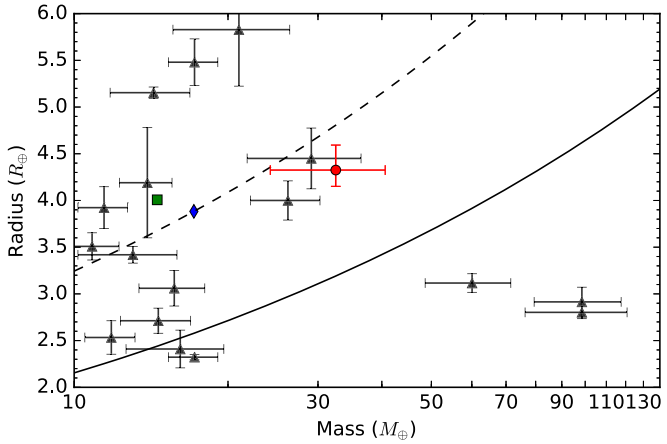

Figure 3. Mass–radius diagram for Neptune-size planets ($2.0 \lesssim R_p \lesssim 6.0\ R_\oplus$) whose mass and radius have both been determined with a precision of at least ~25% (Exoplanet Orbit Database, as of 2016 June; Han et al. 2014). The red circle marks the position of K2-98b. The green diamond and blue square show the position of Neptune and Uranus, respectively. The solid and dashed lines mark the Earth (5.5 g cm^{-3}) and Neptune (1.6 g cm^{-3}) isodensity curves.

equilibrium tide (Ogilvie & Lin 2007). Therefore, we explore the evolution for three fixed values of $Q'_\star$, i.e., 10^5, 10^6, and 10^7, from the stronger to the weaker coupling. Following Lanza et al. (2011), we include the loss of angular momentum produced by the stellar magnetized wind considering a saturation regime for an angular velocity greater than $8\,\Omega_\odot$, where $\Omega_\odot$ is the present solar angular velocity. We assume that the orbit of the planet is circular, although the tidal interaction is so weak that any initial eccentricity could survive up to the present stage of the system evolution (see below).

Figure 4 shows the evolution of the rotation period of the star (upper panel), semimajor axis of the planet's orbit (middle panel), and stellar radius (lower panel) as obtained from the evolutionary models presented in Section 5. Tidal interaction is so weak that there is virtually no evolution of the orbital separation since the planet arrived at the present semimajor axis (Figure 4, middle panel). The rotation of the star is braked solely by the stellar wind with a completely negligible tidal exchange between the orbital and the spin angular momenta, and no dependency on the stellar tidal quality factor $Q'_\star$, owing to the small mass of the planet and large separation. (Figure 4, upper panel). Under our model assumptions, we estimate that the star reached the zero age main sequence (ZAMS) with a rotation period of about 1.5 days.

The tidal evolution of the planet will become important in the future—after ~3 Gyr from now—due to the increase of the stellar radius and rotational period of the star, leading to a rapid decay of the planet's orbit (Figure 4, middle panel).

The amount of angular momentum in the orbit is insufficient to synchronize the rotation of the star, so the present approximately synchronous state cannot be maintained. Damiani & Lanza (2015) showed that other systems having host stars with an effective temperature around 6100 K show a rather wide distribution of the ratio of the orbital period to the stellar spin period, even in the case of more massive planets, thus supporting the conclusion that the present approximate synchronicity is probably coincidental.

Finally, we consider the possibility that the planet was initially significantly closer to the star when the latter reached the ZAMS and was pushed outwards by the action of tides because angular momentum was transferred from the stellar spin to the orbit, provided that the rotational period of the star was shorter than the orbital one. We also find that this scenario

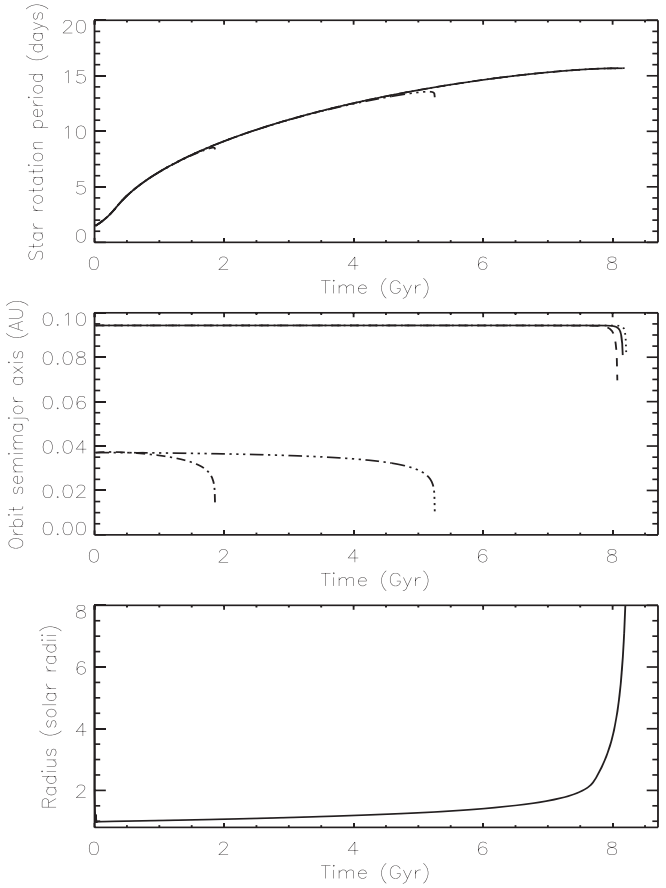

Figure 4. Rotational period of the star (upper panel), semimajor axis of the planet orbit (middle panel), and stellar radius (lower panel) versus time. Different line styles refer to different initial semimajor axis a_0 and tidal quality factor of the star $Q'_\star$ as follows: solid line: $Q'_\star = 10^6$, $a_0 = 0.0943$ au; dotted line: $Q'_\star = 10^7$, $a_0 = 0.0943$ au; dashed line: $Q'_\star = 10^5$, $a_0 = 0.0943$ au; dashed–dotted: $Q'_\star = 10^5$, $a_0 = 0.037$ au (corresponding to an orbital period of 2.5 days); dashed–triple-dotted: $Q'_\star = 10^6$, $a_0 = 0.037$ au.

is unlikely. As an illustrative case, we show in Figure 4 two integrations for the planet initially at an orbital period of 2.5 days, corresponding to a semimajor axis of 0.037 au. This is the minimum orbital period for observed Neptune-mass planets around main-sequence stars (cf. Figure 4 of Valsecchi et al. 2014) that we choose in order to maximize the strength of the tidal interaction. Since the star was initially rotating faster than the planet, the tidal interaction was initially pushing the planet outwards, in particular for $Q'_\star = 10^5$ (Figure 4, middle panel). However, the fast rotational braking of the star soon led to a rotation period longer than the orbital period. Since the amount of orbital angular momentum was too small to maintain the synchronous state, the final fate of the planet was to fall toward the star under the action of tides within a few Gyr.[24] This scenario would account for the significant dearth of Neptune-like planets with orbital periods below 2-4 days (see, e.g., Szabó & Kiss 2011; Mazeh et al. 2016).

[24] We note that assuming a different initial orbital period leads to qualitatively similar scenarios. If the initial orbital period of the planet is shorter than 2.5 days (i.e., $a_0 < 0.037$ au), the tidal push is stronger, but only for a shorter time interval before the rotation period of the star becomes longer than the orbital period, after which the orbit decays faster. If the planet is farther out ($P_{0,\rm orb} > 2.5$ days and $a_0 > 0.037$ au), tides are weaker, but they can act longer before the direction of the evolution of the semimajor axis is reversed and the planet falls into the star.

The tidal evolution of the system further supports an inward migration scenario for K2-98b, from the outer region of the system to its current position.

8. CONCLUSIONS

We confirm the planetary nature of K2-98b and derive the system parameters. Our results are based on photometric data from the *K2* space mission combined with high-precision Tull, FIES, HARPS, and HARPS-N RV measurements and lucky imaging. K2-98b is a transiting Neptune-size planet in a 10 day orbit around an F8 V leaving the main sequence. It has a mass of $M_{\rm p} = 32.2 \pm 8.1$ $M_{\oplus}$ and a radius of $R_{\rm p} = 4.3^{+0.3}_{-0.2}$ $R_{\oplus}$, translating into a mean density of $2.15^{+0.67}_{-0.60}$ g cm^{-3}. K2-98b joins the still relatively small number of Neptune-size planets (~20 objects) whose mass and radius have been determined with a precision better than 25%.

We thank the anonymous referee for the insightful, thoughtful, and constructive review. We are very grateful to Simon Albrecht for providing us with one of the HARPS-N measurement and for his valuable comments and suggestions. We are thankful to Jorge Melendez, Martin Kürster, Nuno Santos, Xavier Bonfils, and François Bouchy who kindly agreed to exchange HARPS time with us. We express our deepest gratitude to the NOT, ESO, TNG, and McDonald staff members for their unique support during the observations. S.C. thanks the Hungarian OTKA Grant K113117. H.J.D. and D.N. acknowledge support by grant ESP2015-65712-C5-4-R of the Spanish Secretary of State for R& D&i (MINECO). This research was supported by the Ministerio de Economia y Competitividad under project FIS2012-31079. The research leading to these results has received funding from the European Union Seventh Framework Programme (FP7/2013-2016) under grant agreement No. 312430 (OPTICON) and from the NASA *K2* Guest Observer Cycle 1 program under grant NNX15AV58G to The University of Texas at Austin. This paper includes data taken at McDonald Observatory of the University of Texas at Austin. Based on observations obtained (a) with the Nordic Optical Telescope (NOT), operated on the island of La Palma jointly by Denmark, Finland, Iceland, Norway, and Sweden, in the Spanish Observatorio del Roque de los Muchachos (ORM) of the Instituto de Astrofísica de Canarias (IAC), and (b) with the Italian Telescopio Nazionale Galileo (TNG) also operated at the ORM (IAC) on the island of La Palma by the INAF—Fundación Galileo Galilei. Based on observations made with ESO Telescopes at La Silla Observatory under programme ID 097.C-0948. This research made use of data acquired with the Carlos Sánchez (TCS) Telescope, operated at Teide Observatory on the island of Tenerife by the Instituto de Astrofísica de Canarias. This paper includes data collected by the *Kepler* mission. Funding for the *Kepler* mission is provided by the NASA Science Mission directorate. This publication makes use of data products from the Two Micron All Sky Survey (2MASS), which is a joint project of the University of Massachusetts and the Infrared Processing and Analysis Center/California Institute of Technology, funded by the National Aeronautics and Space Administration and the National Science Foundation. This publication makes use of data products from the *Wide-field Infrared Survey Explorer* (*WISE*), which is a joint project of the University of California, Los Angeles, and the Jet Propulsion Laboratory/California Institute of Technology, funded by the National Aeronautics and Space Administration.

Facilities: Kepler (*K2*), NOT (FIES), ESO:3.6m (HARPS), Sanchez (FASTCAM), Smith (Tull), TNG (HARPS-N).

Software: `COELI`, `DEBIL`, `DST`, `EXOTRANS`, `Kea IDL`, `IRAF`, `pyaneti`, `SME`, `TAP`.

REFERENCES

Asplund, M., Grevesse, N., Sauval, A. J., & Scott, P. 2009, ARA&A, 47, 481
Baglin, A., Auvergne, M., Boisnard, L., et al. 2006, in 36th COSPAR Scientific Assembly, 36, 3749
Baranne, A., Queloz, D., Mayor, M., et al. 1996, A&AS, 119, 373
Barros, S. C. C., Demangeon, O., & Deleuil, M. 2016, arXiv:1607.02339
Borucki, W. J., Koch, D., Basri, G., et al. 2010, Sci, 327, 977
Borucki, W. J., Koch, D. G., Basri, G., et al. 2011, ApJ, 728, 117
Bruntt, H., Bedding, T. R., Quirion, P.-O., et al. 2010, MNRAS, 405, 1907
Buchhave, L. A., Bakos, G. A., Hartman, J. D., et al. 2010, ApJ, 720, 1118
Cabrera, J., Csizmadia, S., Erikson, A., Rauer, H., & Kirste, S. 2012, A&A, 548, A44
Cabrera, J., Csizmadia, S., Lehmann, H., et al. 2014, ApJ, 781, 18
Cabrera, J., Fridlund, M., Ollivier, M., et al. 2009, A&A, 506, 501
Cagigal, M. P., Valle, P. J., Cagigas, M. A., et al. 2016, MNRAS, 464, 680
Cagigal, M. P., Valle, P. J., Colodro-Conde, C., Villó-Pérez, I., & Pérez-Garrido, A. 2016, MNRAS, 455, 2765
Carone, L., Gandolfi, D., Cabrera, J., et al. 2012, A&A, 538, A112
Carpano, S., Cabrera, J., Alonso, R., et al. 2009, A&A, 506, 491
Cavarroc, C., Moutou, C., Gandolfi, D., et al. 2012, Ap&SS, 337, 511
Claret, A., & Bloemen, S. 2011, A&A, 529, A75
Cochran, W. D., Endl, M., Johnson, M. C., et al. 2015, AAS/Division for Planetary Sciences Meeting Abstracts, 47, 417.02
Cosentino, R., Lovis, C., Pepe, F., et al. 2012, Proc. SPIE, 8446, 1
Csizmadia, S., Pasternacki, T., Dreyer, C., et al. 2013, A&A, 549, A9
Cutri, R. M., Skrutskie, M. F., van Dyk, S., et al. 2003, 2MASS All-Sky Catalog of Point Sources (NASA/IPAC Infrared Science Archive)
Cutri, R. M., et al. 2013, yCat, 2328, 0
Damiani, C., & Lanza, A. F. 2015, A&A, 574, A39
David, T. J., Hillenbrand, L. A., Petigura, E. A., et al. 2016, Natur, 534, 658
Dell'Omodarme, M., Valle, G., Degl'Innocenti, S., & Prada Moroni, P. G. 2012, A&A, 540, A26
Devor, J. 2005, ApJ, 628, 411
Doyle, A. P., Davies, G. R., Smalley, B., Chaplin, W. J., & Elsworth, Y. 2014, MNRAS, 444, 3592
Endl, M., & Cochran, W. D. 2016, PASP, 128, 094502
Erikson, A., Santerne, A., Renner, S., et al. 2012, A&A, 539, A14
Espinoza, N., Brahm, R., Jordán, A., et al. 2016, arXiv:1601.07608
Ford, E. B., Rowe, J. F., Fabrycky, D. C., et al. 2011, ApJS, 197, 2
Frandsen, S., & Lindberg, B. 1999, in Proc. Anot. Conf. 71, Astrophysics with the NOT, ed. H. Karttunen & V. Piirola (Piikkio: University of Turku)
Fridlund, M., Hébrard, G., Alonso, R., et al. 2010, A&A, 512, A14
Gandolfi, D., Hébrard, G., Alonso, R., et al. 2010, A&A, 524, A55
Gandolfi, D., Parviainen, H., Deeg, H. J., et al. 2015, A&A, 576, A11
Gandolfi, D., Parviainen, H., Fridlund, M., et al. 2013, A&A, 557, A74
Gandolfi, D., Alcalá, J. M., Leccia, S., et al. 2008, ApJ, 687, 1303
Gazak, J. Z., Johnson, J. A., Tonry, J., et al. 2012, AdAst, 2012, 697967
Goodman, J., & Weare, J. 2010, Comm. App. Math. Comp. Sci., 5, 65
Gregory, P. 2010, in Bayesian Logical Data Analysis for the Physical Sciences, ed. P. Gregory (Cambridge, UK: Cambridge Univ. Press), 312
Grziwa, S., Gandolfi, D., Csizmadia, S., et al. 2015, arXiv:1510.09149
Grziwa, S., & Pätzold, M. 2016, arXiv:1607.08417
Grziwa, S., Pätzold, M., & Carone, L. 2012, MNRAS, 420, 1045
Gustafsson, B., Edvardsson, B., Eriksson, K., et al. 2008, A&A, 486, 951
Han, E., Wang, S. X., Wright, J. T., et al. 2014, PASP, 126, 827
Hatzes, A. P. 2016, SSRv
Hauschildt, P. H., Allard, F., & Baron, E. 1999, ApJ, 512, 377
Howell, S. B., Sobeck, C., Haas, M., et al. 2014, PASP, 126, 398
Johnson, M. C., Gandolfi, D., Fridlund, M., et al. 2016, AJ, 151, 171
Kipping, D. M. 2010, MNRAS, 408, 1758
Kipping, D. M. 2013, MNRAS, 435, 2152
Kley, W., & Nelson, R. P. 2012, ARA&A, 50, 211
Kovács, G., Zucker, S., & Mazeh, T. 2002, A&A, 391, 369
Kurucz, R. 1993, ATLAS9 Stellar Atmosphere Programs and 2 km/s grid. Kurucz CD-ROM No. 13 (Cambridge, MA: Smithsonian Astrophysical Observatory)

Kurucz, R. L. 2013, ATLAS12: Opacity sampling model atmosphere program, Astrophysics Source Code Library, ascl:1303.024
Lanza, A. F., Damiani, C., & Gandolfi, D. 2011, A&A, 529, A50
Lanza, A. F., & Mathis, S. 2016, arXiv:1606.08623
Lucy, L. B., & Sweeney, M. A. 1971, AJ, 76, 544
Mandel, K., & Agol, E. 2002, ApJL, 580, L171
Marcy, G. W., Weiss, L. M., Petigura, E. A., et al. 2014, PNAS, 111, 12655
Mayor, M., Pepe, F., Queloz, D., et al. 2003, Msngr, 114, 20
Mayor, M., & Queloz, D. 1995, Natur, 378, 355
Mazeh, T., Holczer, T., & Faigler, S. 2016, A&A, 589, A75
Nespral, D., Gandolfi, D., Deeg, H. J., et al. 2016, arXiv:1604.01265
Ogilvie, G. I., & Lin, D. N. C. 2007, ApJ, 661, 1180
Oscoz, A., Rebolo, R., López, R., et al. 2008, Proc. SPIE, 7014, 701447
Pätzold, M., Endl, M., Csizmadia, S., et al. 2012, A&A, 545, A6
Pepe, F., Mayor, M., Galland, F., et al. 2002, A&A, 388, 632
Perryman, M. 2014, in The Exoplanet Handbook, ed. M. Perryman (Cambridge, UK: Cambridge Univ. Press)
Pope, B. J. S., Parviainen, H., & Aigrain, S. 2016, MNRAS, 461, 3399
Prsa, A., Harmanec, P., Torres, G., et al. 2016, arXiv:1605.09788
Sanchis-Ojeda, R., Rappaport, S., Pallè, E., et al. 2015, ApJ, 812, 112
Schlichting, H. E. 2014, ApJL, 795, L15
Straizys, V., & Kuriliene, G. 1981, Ap&SS, 80, 353
Szabó, G. M., & Kiss, L. L. 2011, ApJL, 727, L44
Telting, J. H., Avila, G., Buchhave, L., et al. 2014, AN, 335, 41
Thoul, A. A., Bahcall, J. N., & Loeb, A. 1994, ApJ, 421, 828
Tognelli, E., Prada Moroni, P. G., & Degl'Innocenti, S. 2011, A&A, 533, A109
Tull, R. G., MacQueen, P. J., Sneden, C., & Lambert, D. L. 1995, PASP, 107, 251
Udry, S., Mayor, M., & Queloz, D. 1999, ASPC, 185, 367
Valenti, J. A., & Fischer, D. A. 2005, ApJS, 159, 141
Valenti, J. A., & Piskunov, N. 1996, A&AS, 118, 595
Valsecchi, F., Rasio, F. A., & Steffen, J. H. 2014, ApJL, 793, L3
Vanderburg, A., & Johnson, J. A. 2014, PASP, 126, 948
Wallace, L., Hinkle, K. H., Livingston, W. C., & Davis, S. P. 2011, ApJS, 195, 6
Weiss, L. M., & Marcy, G. W. 2014, ApJL, 783, L6
Winn, J. N., & Fabrycky, D. C. 2015, ARA&A, 53, 409
Zacharias, N., Urban, S. E., Zacharias, M. I., et al. 2004, AJ, 127, 3043